ChemSusChem

Research Article
doi.org/10.1002/cssc.202501192

Chemistry Europe
European Chemical Societies Publishing

www.chemsuschem.org

VIP Very Important Paper

Modulating Lithium-Ion Transport in $LiAlBr_4$ via S-Modified Anion Sublattice

Ifeoluwa P. Oyekunle, Tej P. Poudel, Yudan Chen, Erica Truong, Islamiyat A. Ojelade, Pawan K. Ojha, Md. Mahinur Islam, Yongkang Jin, and Yan-Yan Hu*

Tailoring the structures or chemical compositions of the host lattice modulates cation–anion interactions, enhancing active cation transport. Herein, a Br-S mixed-anion sublattice in $LiAlBr_4$ lowers the migration energy barrier, facilitating lithium redistribution, and enhanced ionic conductivity in $Li_{1.2}AlBr_{3.8}S_{0.2}$. Ab initio molecular dynamics simulations reveal restricted diffusion in $LiAlBr_4$, whereas $Li_{1.2}AlBr_{3.8}S_{0.2}$ features a delocalized network indicative of improved macroscopic Li^+ transport. $Li_{1.2}AlBr_{3.8}S_{0.2}$ exhibits excellent cycling stability and rate capability in all-solid-state batteries, delivering a high specific capacity of 150.2 mAh g^{-1} at 2C in a Li-In|Li_6PS_5Cl|2($Li_{1.2}AlBr_{3.8}S_{0.2}$): TiS_2 cell, outperforming the $LiAlBr_4$-based system (45.2 mAh g^{-1}) under the same conditions. These findings offer key insights into structure-ion transport relationships, enabling the design of high-performance solid electrolytes.

1. Introduction

The rapid growth of the electric vehicle industry is driving a surge in demand for advanced energy storage technologies.[1–4] All-solid-state lithium batteries (ASSBs), which utilize nonflammable solid electrolytes (SEs), are gaining prominence as next-generation energy storage solutions due to their high theoretical energy density and improved safety profiles.[5–13] An ideal SE should combine cost-effectiveness,[14,15] high ionic conductivity,[14,16–18] negligible electronic conductivity,[19] favorable mechanical properties,[17,20] robust structural stability, and compatibility with electrodes across wide electrochemical and thermal ranges.[18,20] However, while meeting these criteria, SEs that exhibit high Li^+ conductivity ($\geq 10^{-4}$ S cm^{-1} at room temperature) remain scarce.[21]

Lithium tetrahaloaluminates, $LiAlX_4$ (X = Cl, Br, I), are considered a promising class of SEs owing to their thermal and electrochemical oxidative stability, cost-effectiveness, and good mechanical properties.[22–24] Nevertheless, their ionic conductivity is relatively low (≤ 0.03 mS cm^{-1}), limiting their practical use in ASSBs.[22,23] The anions and their arrangements within the host sublattice are fundamental to Li^+-ion conduction.[20,25] Minor changes to the anion substructure can introduce static and dynamic disorder, which notably affects ion mobility.[23,26–29] Additionally, a mixed-anion sublattice incorporating multiple anions has been found to improve cation conduction by modulating cation–anion interactions.[23,27,28]

Recent research has shown that combining low-cost, poor-conducting Li_2S with $AlCl_3$ can enhance Li^+ conduction in $LiAlCl_4$. The increased ionic conductivity results from the formation of a Cl-S mixed-anion sublattice, which generates interconnected face- and edge-sharing octahedra structures, establishing 3D ion conduction pathways with lower activation energy barriers.[23]

Herein, we examined the influence of anion substitution on Li^+ transport in $LiAlBr_4$. Our findings revealed a significant enhancement in room-temperature ionic conductivity, achieving 0.2 mS cm^{-1} for $Li_{1.2}AlBr_{3.8}S_{0.2}$, which is over twenty times higher than the ionic conductivity of $LiAlBr_4$. Multimodal structural and ion dynamics characterization revealed that partial substitution of Br^- with S^{2-} in $LiAlBr_4$ enhances polyhedral connectivity, induces Li^+ redistribution, and reduces the activation energy barrier for Li^+ transport. These synergistic effects significantly change transport pathways, yielding improved ionic conductivity.

2. Results and Discussion

The average structures of $LiAlBr_4$ and $Li_{1.2}AlBr_{3.8}S_{0.2}$ were analyzed using powder X-ray diffraction (PXRD) (**Figure 1**a,b). The difference in the XRD patterns of $LiAlBr_4$ and $Li_{1.2}AlBr_{3.8}S_{0.2}$ is evident: the weak diffraction peaks of $Li_{1.2}AlBr_{3.8}S_{0.2}$ indicate reduced crystallinity. Rietveld refinement of the diffraction data (Figure 1c–f) confirmed that both compounds adopt a monoclinic crystal structure belonging to the $P2_1/a$ space group. A detailed structural description of $LiAlX_4$ (X = Cl, Br, I) has been previously reported.[22,23] $LiAlBr_4$ is characterized by a fully occupied corner-sharing Li site, Li_{4e} (Figure 1e), and the absence of vacancies in

---

I. P. Oyekunle, T. P. Poudel, Y. Chen, E. Truong, I. A. Ojelade, P. K. Ojha, M. M. Islam, Y. Jin, Y.-Y. Hu
Department of Chemistry and Biochemistry
Florida State University
Tallahassee, FL 32306, USA
E-mail: yhu@fsu.edu

I. P. Oyekunle, T. P. Poudel, Y. Chen, E. Truong, I. A. Ojelade, P. K. Ojha, M. M. Islam, Y. Jin, Y.-Y. Hu
Centre for Interdisciplinary Magnetic Resonance
National High Filed Magnetic Laboratory
Tallahassee, FL 32310, USA

T. P. Poudel, Y.-Y. Hu
Materials Science and Engineering Program
Florida State University
Tallahassee, FL 32306, USA

Supporting information for this article is available on the WWW under https://doi.org/10.1002/cssc.202501192

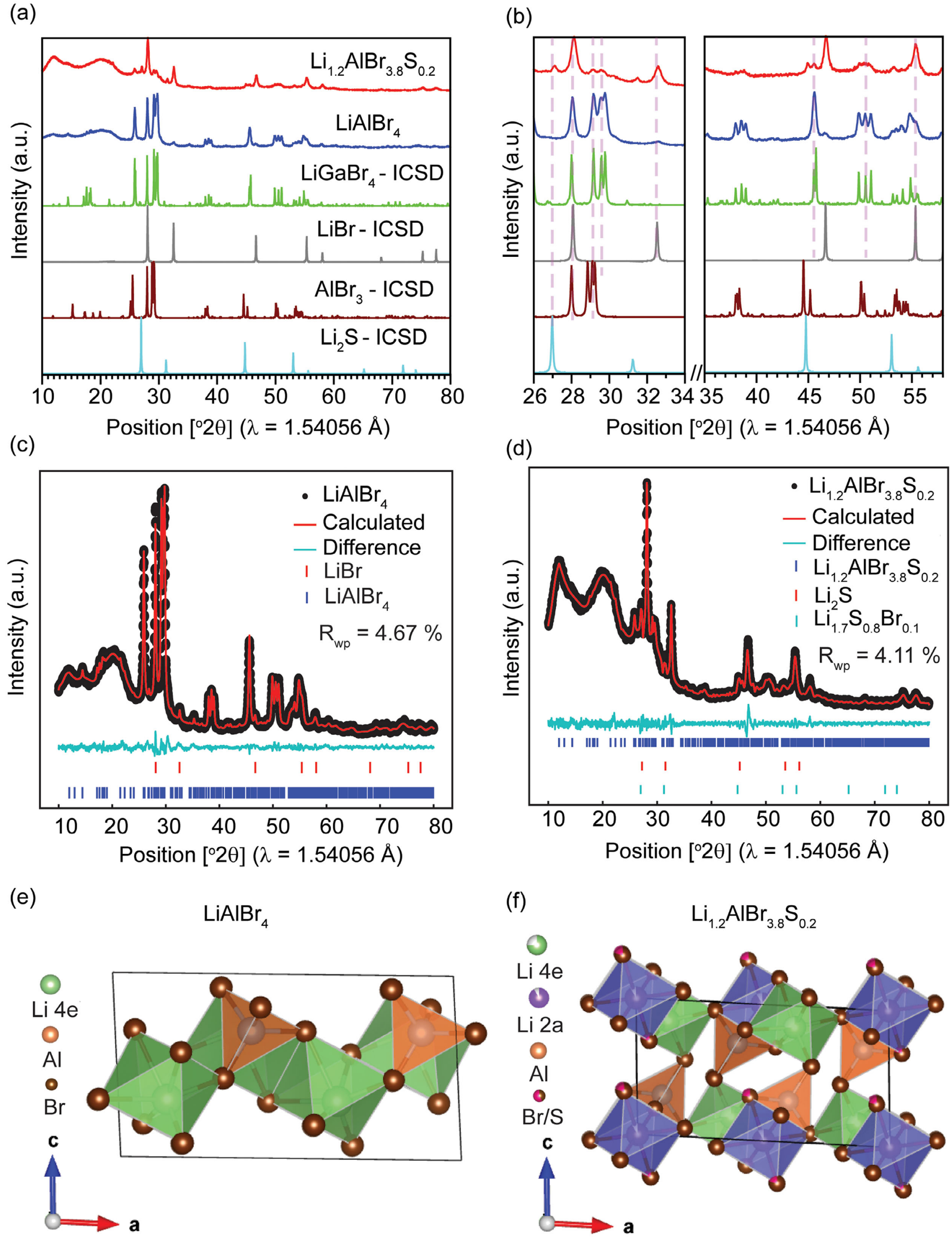

Figure 1. Long-range structures of $LiAlBr_4$ and $Li_{1.2}AlBr_{3.8}S_{0.2}$, determined using PXRD. a) PXRD patterns of the as-milled $LiAlBr_4$ and $Li_{1.2}AlBr_{3.8}S_{0.2}$. The inorganic crystal structure database (ICSD) patterns of precursors and $LiAlBr_4$ monoclinic phase ($P2_1/a$ space group) are shown as references. b) The magnified view of the selected 2θ ranges in (a). c,d) PXRD patterns and the corresponding Rietveld refinement of $LiAlBr_4$ and $Li_{1.2}AlBr_{3.8}S_{0.2}$, respectively. e) and, f) Monoclinic structures of $LiAlBr_4$ and $Li_{1.2}AlBr_{3.8}S_{0.2}$ with the $P2_1/a$ space group, respectively, obtained from the Rietveld refinement of the XRD patterns.

$LiAlBr_4$ limits Li^+-ion mobility. $Li_{1.2}AlBr_{3.8}S_{0.2}$ features a 3D framework with $AlBr_4$ tetrahedral and $LiBr_xS_y$ octahedra. S^{2-} partially replaced Br^- in the 4e Wyckoff site, creating a disordered anion sublattice, with Li^+ occupying both 4e and 2a Wyckoff sites.

The structural transformation introduces additional crystallographic sites (Li_{2a}) for Li^+ incorporation. Lithium-ions occupying these newly accessible sites exhibit markedly higher mobility compared to those in $LiAlBr_4$, where Li sites are fully occupied. This enhanced mobility is evidenced by NMR T_1 relaxation time measurements. The combination of increased Li^+ mobility and a higher charge carrier concentration results in a marked enhancement in the lithium-ion conductivity of $Li_{1.2}AlBr_{3.8}S_{0.2}$. The refined

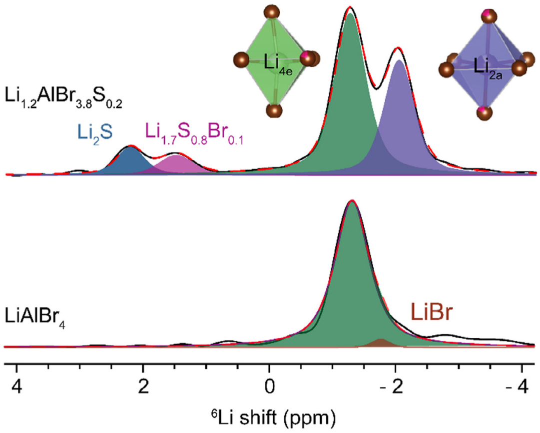

Figure 2. ^{6}Li MAS NMR spectra of $LiAlBr_4$ and $Li_{1.2}AlBr_{3.8}S_{0.2}$.

unit cell parameters for $LiAlBr_4$ and $Li_{1.2}AlBr_{3.8}S_{0.2}$ are provided in Tables S1, S2, and S3, Supporting Information.

NMR spectroscopy and T_1 relaxation time measurements were utilized to study the influence of anion substitution on Li^+-ion local environments and dynamics in $LiAlBr_4$ and $Li_{1.2}AlBr_{3.8}S_{0.2}$. **Figure 2** shows the ^{6}Li MAS NMR spectra of $LiAlBr_4$ and $Li_{1.2}AlBr_{3.8}S_{0.2}$. $LiAlBr_4$ is characterized by a major resonance at −1.25 ppm, and a minor resonance from LiBr impurity. Diversifying the anion sublattice resulted in the redistribution of Li^+ ions, evident by the formation of a new Li_{2a} site (−2.01 ppm) in addition to the Li_{4e} site in $Li_{1.2}AlBr_{3.8}S_{0.2}$. Minor Li_2S impurity and a $Li_{1.7}S_{0.8}Br_{0.1}$ phase were observed at 2.23 ppm and 1.54 ppm, respectively. The resonance at $Li_{1.7}S_{0.8}Br_{0.1}$, also observed from structural refinement of the XRD, is attributed to a secondary phase formed from local compositional variations or phase segregation during synthesis. The low Br^- content in $Li_{1.7}S_{0.8}Br_{0.1}$ slightly perturbs the chemical environment while maintaining structural similarity to Li_2S, causing its resonance to appear near the Li_2S peak. This reflects their compositional and structural resemblance. The quantified phase composition is presented in Table S4, Supporting Information.

A quantitative assessment of Li^+-ion dynamics was conducted through ^{7}Li spin-lattice (T_1) relaxation time measurements. The Bloembergen, Purcell, and Pound model relates the motional correlation time (τ_c) to the spin relaxation time.[30] The relationship between T_1 and τ_c is given by $\frac{1}{T_1} = \frac{3\gamma^4\hbar^2}{10r_0^6}\left[\frac{\tau_c}{1+\omega_0^2\tau_c^2} + \frac{4\tau_c}{1+4\omega_0^2\tau_c^2}\right]$, where γ is the magnetogyric ratio, μ_0 is the vacuum permeability, $\hbar$ is the reduced Planck constant, r_0 is the interatomic distance, and ω_0 is the Larmor frequency. In the fast-motion regime ($\omega_0\tau_c \ll 1$),

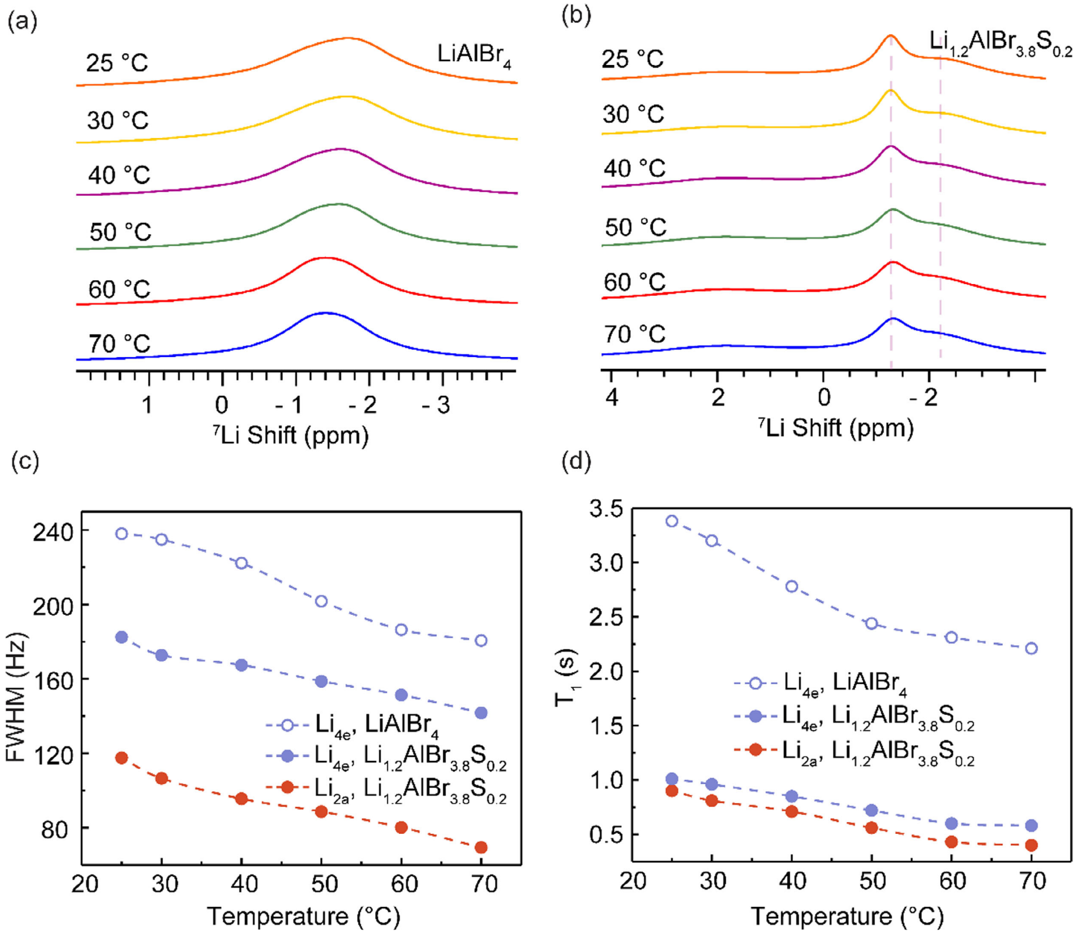

Figure 3. ^{7}Li VT NMR spectra of a) $LiAlBr_4$ b) $Li_{1.2}AlBr_{3.8}S_{0.2}$. c) ^{7}Li NMR line widths as a function of temperature for $LiAlBr_4$ and $Li_{1.2}AlBr_{3.8}S_{0.2}$. d) ^{7}Li NMR T_1 of $LiAlBr_4$ and $Li_{1.2}AlBr_{3.8}S_{0.2}$ as a function of temperature to probe ion dynamics.

T_1 increases with increasing motional rate, while in the slow-motion regime ($\omega_0\tau_c \gg 1$), T_1 decreases with increasing motional rate.[31] Temperature-dependent NMR measurements of $LiAlBr_4$ and $Li_{1.2}AlBr_{3.8}S_{0.2}$ reveal a decrease in the T_1 relaxation time with increasing temperature (**Figure 3**). This indicates that Li^+ ion motion lies in the slow-motion regime, where $\omega_0\tau_c \gg 1$.[32] Moreso, the peak width narrows with S^{2-} incorporation, indicating enhanced Li^+ dynamics in $Li_{1.2}AlBr_{3.8}S_{0.2}$ that average out homogeneous and inhomogeneous line broadening (Figure 3c). At room temperature, ^7Li T_1 relaxation measurements revealed a shorter T_1 of ≈1.0 s for $Li_{1.2}AlBr_{3.8}S_{0.2}$, compared to 3.4 s for $LiAlBr_4$, indicating enhanced Li^+ dynamics in $Li_{1.2}AlBr_{3.8}S_{0.2}$ (Figure 3d & Table S5, Supporting Information). Notably, the T_1 trend aligns with the observed line-narrowing behavior, highlighting the correlation between sharper resonances, shorter T_1, and increased ion mobility.[33,34]

Ab initio molecular dynamics (AIMD) simulations were performed for $LiAlBr_4$ and $Li_{1.2}AlBr_{3.8}S_{0.2}$ to explore how S^{2-} incorporation influences the structure and Li^+ transport. The mean square displacements (MSD) of Li^+ and Li^+ density probability maps at 900 K are presented in **Figure 4**. MSD plots show Li^+ diffusion in all directions, with dominant c-axis diffusion in $LiAlBr_4$. Notably, Br-S substitution enhances a- and b-axis diffusion in $Li_{1.2}AlBr_{3.8}S_{0.2}$, with ≈100% enhancement in the overall MSD of Li^+ compared to $LiAlBr_4$. The Li^+ probability density maps reveal confined Li^+ diffusion in $LiAlBr_4$, while $Li_{1.2}AlBr_{3.8}S_{0.2}$ exhibits a delocalized network, signifying enhanced macroscopic Li^+ migration.

The ionic conductivities of $LiAlBr_4$, $Li_{1.2}AlBr_{3.8}S_{0.2}$, and Li_5AlS_4 were assessed using electrochemical impedance spectroscopy (EIS), with the Nyquist plots at 25 °C displayed in **Figure 5**a. The ionic conductivity is determined from the bulk impedance resistance using $\sigma_{DC} = L/(R \times A)$, where L is the pellet thickness, A is the electrode surface area, and R is the resistance obtained from the equivalent circuit fitting of the Nyquist plots. Ionic conductivities of 0.009 mS cm^{-1} and 0.20 mS cm^{-1} were obtained for $LiAlBr_4$ and $Li_{1.2}AlBr_{3.8}S_{0.2}$, respectively. Moreover, at $x = 0.1$, 0.3, 0.4, and 0.5, ionic conductivities of 0.18, 0.16, 0.15, and 0.13 mS cm^{-1} were obtained for the $Li_{1+x}AlBr_{4-x}S_x$ series (Figure S1, Supporting Information). The low conductivity at $x = 0.1$ likely stems from insufficient sulfur incorporation to significantly modify the lattice and enhance Li^+ transport pathways, and beyond $x = 0.2$, the decreased conductivity observed with higher S content is likely due to the exceeded solid-solution limit, leading to increased Li_2S impurity that impedes ion transport (Figure S2, Supporting Information). With the complete replacement of Br^-, Li_5AlS_4 demonstrates a lower ionic conductivity of 1.7×10^{-5} mS cm^{-1}. The composition, $Li_{1.2}AlBr_{3.8}S_{0.2}$, was identified as optimal for maximizing ionic conductivity. This highlights the role of a Br-S mixed anion system in creating a structural framework that facilitates Li^+ transport. The representative Nyquist plot of $Li_{1.2}AlBr_{3.8}S_{0.2}$ fitted to the data collected at 0 °C is shown in Figure 5b. The high-frequency

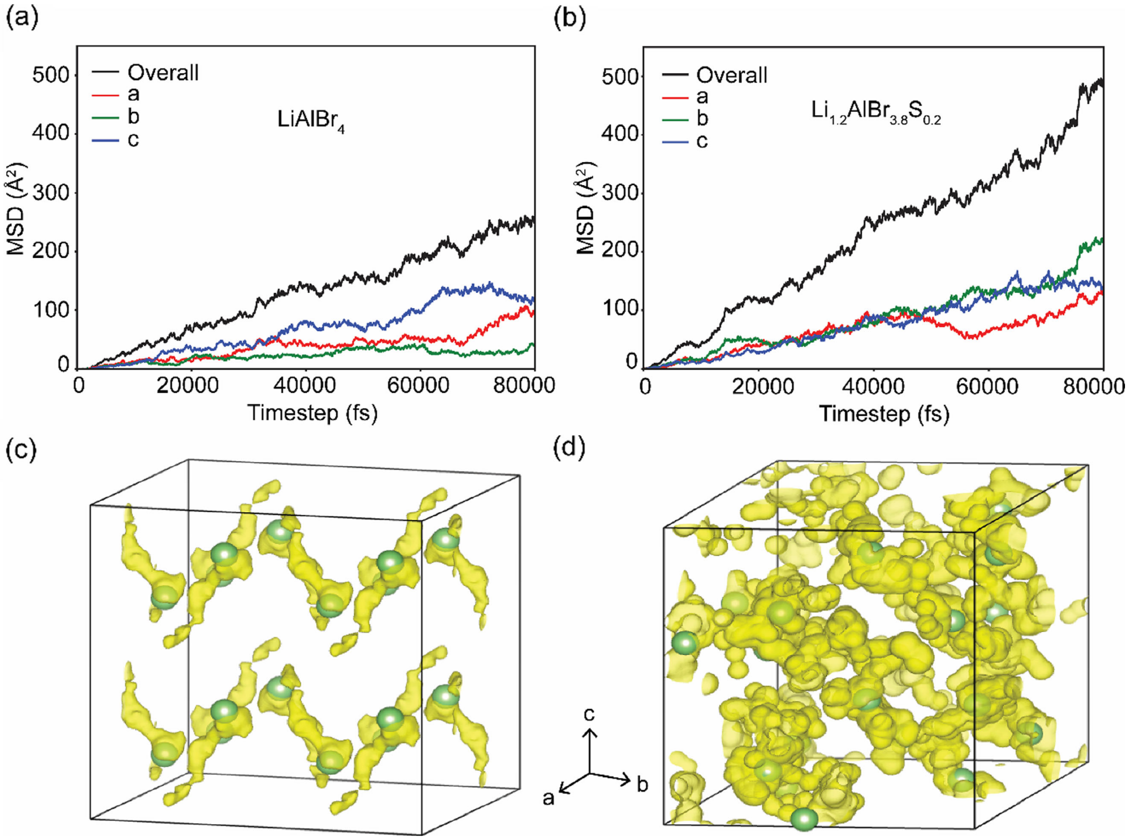

Figure 4. MSD of Li^+ in a) $LiAlBr_4$ and b) $Li_{1.2}AlBr_{3.8}S_{0.2}$ generated from AIMD simulations. Li^+ (yellow) probability density map of c) $LiAlBr_4$ and d) $Li_{1.2}AlBr_{3.8}S_{0.2}$ in a $2 \times 2 \times 1$ cell based on AIMD simulations at 900 K.

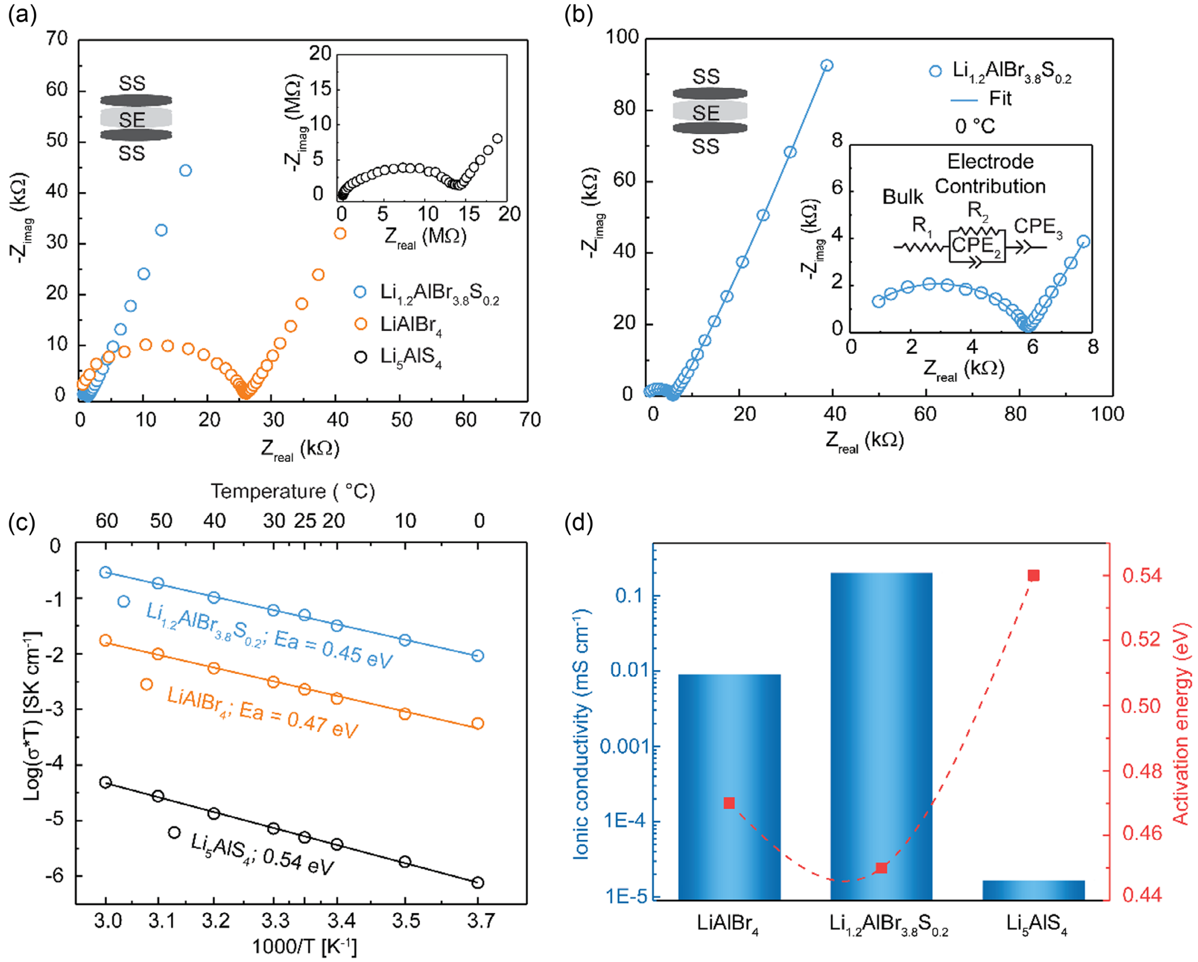

Figure 5. Charge transport properties of $LiAlBr_4$ and $Li_{1.2}AlBr_{3.8}S_{0.2}$. a) Nyquist plots of $LiAlBr_4$ and $Li_{1.2}AlBr_{3.8}S_{0.2}$. b) Exemplary equivalent circuit fitting of the Nyquist plot for $Li_{1.2}AlBr_{3.8}S_{0.2}$ measured at 25 C. c) Ionic conductivity and activation energy of $LiAlBr_4$, $Li_{1.2}AlBr_{3.8}S_{0.2}$, and Li_5AlS_4, and d) Arrhenius plots and activation energies for ion transport in $LiAlBr_4$, $Li_{1.2}AlBr_{3.8}S_{0.2}$, and Li_5AlS_4.

semicircle corresponds to ion transport within the SE, while the low-frequency semicircle reflects the electrode contribution.[35–38]

To contextualize this result, we compared its ionic conductivity with those of previously reported aluminum-containing Li^+- and Na^+-ion conductors. As shown in Table S6, Supporting Information, $Li_{1.2}AlBr_{3.8}S_{0.2}$ exhibits notably higher conductivity than many related systems, underscoring the effectiveness of partial S^{2-} substitution in enhancing Li^+ transport. Moreover, we investigated anion substitution with Cl^- to assess whether similar conductivity improvements could be achieved. However, attempts to introduce Cl^- into the $LiAlBr_{4-x}Cl_x$ series yielded significantly lower ionic conductivities: 0.01, 0.02, and 0.007 mS cm^{-1} for $x = 0.1$, 0.3, and 0.5, respectively (Figure S1, Supporting Information). These poor transport properties suggest that Cl^- substitution does not effectively perturb the lattice to enhance LI^+ transport.

Variable-temperature EIS (VT-EIS) was conducted, with representative Nyquist plots for $LiAlBr_4$ and $Li_{1.2}AlBr_{3.8}S_{0.2}$ shown in Figure S3, Supporting Information. Conductivity across the 0–60 °C range was determined using resistance values obtained from equivalent circuit fitting, and the activation energy for each composition was determined from the slope of the Arrhenius plot (Figure 5c). The activation energies are 0.54 eV for Li_5AlS_4, 0.47 eV for $LiAlBr_4$, and 0.45 eV for $Li_{1.2}AlBr_{3.8}S_{0.2}$. The decrease in activation energy correlates with the observed enhancement in room-temperature conductivity (Figure 5d). The observed trend is consistent with the energy barrier derived from the bond valence site energy calculations, as illustrated in Figure S4, Supporting Information. The DC polarization method was employed to determine the electronic conductivity of the SEs. Electronic conductivities of 8.04×10^{-9} S cm^{-1} and 4.44×10^{-9} S cm^{-1} were obtained for $LiAlBr_4$ and $Li_{1.2}AlBr_{3.8}S_{0.2}$, respectively, confirming that the total measured conductivities are predominantly ionic with minimal electronic contribution (Figure S5, Supporting Information).

Cyclic voltammetry was employed to evaluate the electrochemical stability window of $LiAlBr_4$ and $Li_{1.2}AlBr_{3.8}S_{0.2}$. The electrochemical stability window of $LiAlBr_4$ is theoretically estimated to lie between 1.8 V and 3.9 V versus Li^+/Li (1.2 – 3.3 V vs Li-In).[22,39] **Figure 6** presents the cyclic voltammograms of cells containing $LiAlBr_4$ and $Li_{1.2}AlBr_{3.8}S_{0.2}$, respectively. The anodic peak observed at ≈0.6 V versus Li–In is attributed to the lithiation of carbon.[31] Beyond the stability window, $LiAlBr_4$ is predicted to

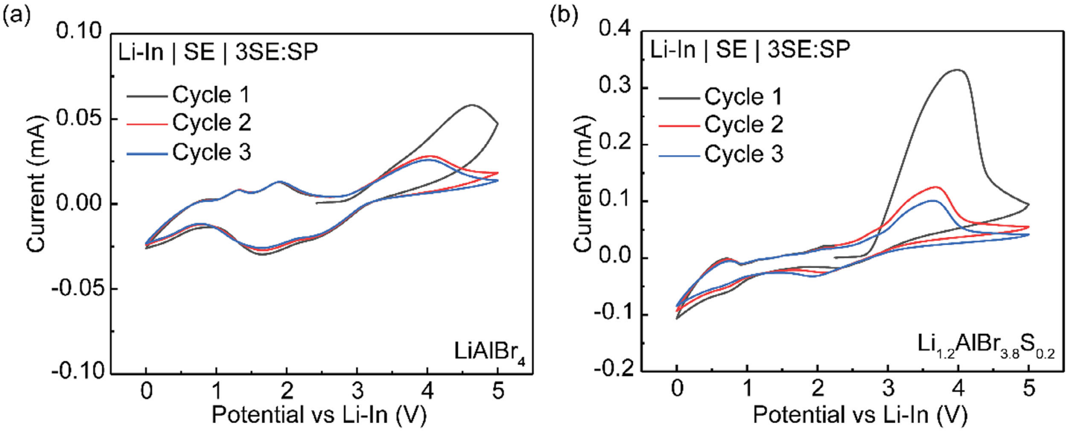

Figure 6. Cyclic voltammograms of Li–In|SE|3SE:SP half-cells over 0–5 V range versus Li–In. CV cycles for a) the $LiAlBr_4$-based cell and b) the $Li_{1.2}AlBr_{3.8}S_{0.2}$-based cell.

decompose to $AlBr_3$ and Br_2 upon oxidation, and to Al and LiBr upon reduction.[22] A pair of redox peaks was observed at ≈2.0 V versus Li–In, corresponding to the Br^-/Br_3^- redox couple. Similar redox behavior has been observed in analogous systems and is associated with the intermediate formation and reduction of tribromide species prior to full Br_2 evolution.[40,41] At a higher oxidation voltage of ≈3.44 V versus Li–In, the anodic peak observed in $LiAlBr_4$ and $Li_{1.2}AlBr_{3.8}S_{0.2}$ is attributed to the complete oxidation of Br_3^- to Br_2.[40] Although this peak is more prominent in the first cycle, it significantly decreased in subsequent cycles, likely due to the formation of a passivation layer. Based on the onset oxidation and reduction voltage, the stability window of $LiAlBr_4$ and $Li_{1.2}AlBr_{3.8}S_{0.2}$ was estimated to be from 1.0 to 3.2 V versus Li–In. This shows that incorporating S^{2-} in the anion sublattice of $LiAlBr_4$ does not significantly alter the electrochemical stability window, as reflected by the identical onset voltages for reduction and oxidation peaks in both the forward and reverse scans.

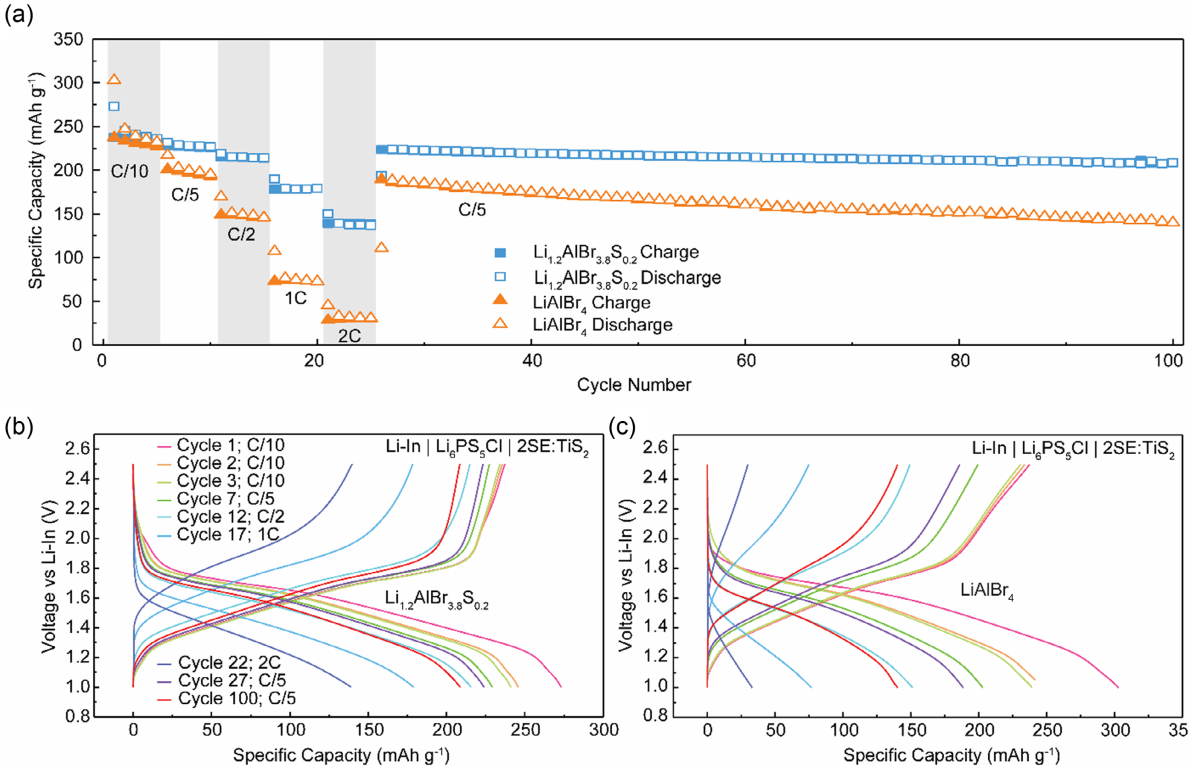

Figure 7. Galvanostatic cycling of 2SE:TiS_2 catholyte with argyrodite (Li_6PS_5Cl) as the separator. a) Rate performance of the Li-In|Li_6PS_5Cl|2SE:TiS_2 cell (SE = $LiAlBr_4$ or $Li_{1.2}AlBr_{3.8}S_{0.2}$) followed by long-term cycling at C/5, where C = 239 mAh g^{-1}. Voltage profile of Cycle 1 along with the 2nd cycles of each C-rate for a b) Li-In|Li_6PS_5Cl|2($Li_{1.2}AlBr_{3.8}S_{0.2}$):$TiS_2$ cell and c) Li-In| Li_6PS_5Cl|2($LiAlBr_4$):TiS_2 cell.

Galvanostatic cycling was performed at 22 °C to assess the performance of half-cells employing $LiAlBr_4$ and $Li_{1.2}AlBr_{3.8}S_{0.2}$, across various C-rates within a voltage window of 1–2.5 V versus Li/In. The charge–discharge rates were calculated based on the theoretical capacity of TiS_2 (239 mAh g^{-1}). Figure S6, Supporting Information, shows their Nyquist plots of the half-cell solid-state batteries and the fitted equivalent circuits. Resistive contributions from the separator, the cathode active material (CAM)–SE interface (CAM/SE), the separator–catholyte (Separator|Catholyte) interface, and the separator|Li–In alloy interface were extracted and are presented in Table S7, Supporting Information. The CAM/SE interfacial resistance is markedly reduced in the $2(Li_{1.2}AlBr_{3.8}S_{0.2})$:$TiS_2$ cell (11.2 Ω) compared to the $2LiAlBr_4$:TiS_2 cell (73.2 Ω). In addition, the separator–catholyte interfacial resistance is significantly lower for the $2(Li_{1.2}AlBr_{3.8}S_{0.2})$:$TiS_2$ cell (35.5 Ω) compared to the $2LiAlBr_4$:TiS_2 cell (99.7 Ω). This confirms that incorporation of sulfur into the halide framework improves interfacial compatibility of the SE with TiS_2.

Figure 7a shows the specific capacity as a function of cycle number for Li-In|Li_6PS_5Cl|$2(LiAlBr_4)$:TiS_2 and Li-In|Li_6PS_5Cl|$2(Li_{1.2}AlBr_{3.8}S_{0.2})$:$TiS_2$ half-cells, with the corresponding voltage profiles for selected cycles provided in Figure 7b,c. The cells were tested for rate performance at C-rates of 0.1, 0.2, 0.5, 1, and 2 C, with the cells cycled five times at each rate, followed by 75 additional cycles at 0.2 C. For $LiAlBr_4$, the initial discharge capacities recorded were 302.8, 217.1, 169.6, 107.2, and 45.2 mAh g^{-1} at 0.1, 0.2, 0.5, 1, and 2 C, respectively. In comparison, the $Li_{1.2}AlBr_{3.8}S_{0.2}$ cell achieved initial discharge capacities of 273.1, 231.7, 218.9, 189.9, and 150.2 mAh g^{-1} for the same C-rates. Notably, the initial discharge capacities of both cells exceeded the theoretical capacity of TiS_2 (239 mAh g^{-1}). This is attributed to additional redox activities within the SE alongside the Ti^{3+}/Ti^{4+} redox (Figure S7, Supporting Information).[23,36,42,43] Both cells exhibited impressive rate performance; however, the $Li_{1.2}AlBr_{3.8}S_{0.2}$-based cell outperformed the $LiAlBr_4$-based cell, delivering a higher capacity of 150.2 mAh g^{-1} compared to 45.2 mAh g^{-1} at a discharge rate of 2 C. Upon reverting to 0.2 C after 25 cycles, both cells exhibited excellent stability over 75 cycles. The $Li_{1.2}AlBr_{3.8}S_{0.2}$-based cell retained about 91% of its capacity between the 26th and 100th cycle, while the $LiAlBr_4$-based cell experienced a faster capacity decline, with 75% capacity retention. The superior performance of the $Li_{1.2}AlBr_{3.8}S_{0.2}$-based cell is attributed to the enhanced ionic conductivity, better interfacial compatibility, and more efficient utilization of the CAM.[23,36]

3. Conclusion

In this work, we demonstrated that partial substitution of Br^- with S^{2-} significantly enhanced Li^+ diffusion in $LiAlBr_4$. $Li_{1.2}AlBr_{3.8}S_{0.2}$ achieved a room-temperature ionic conductivity of 0.20 mS cm^{-1} and an activation energy of 0.45 eV, outperforming $LiAlBr_4$ (0.009 mS cm^{-1}, 0.47 eV). Structural and ion dynamics analyses revealed additional Li^+ sites (Li_{2a}) with significantly higher mobility than those in fully occupied $LiAlBr_4$, facilitating enhanced Li^+ transport in $Li_{1.2}AlBr_{3.8}S_{0.2}$. $Li_{1.2}AlBr_{3.8}S_{0.2}$ half-cell exhibited superior rate performance and cycling stability, attributed to improved ionic conductivity, better interfacial compatibility, and optimized utilization of the CAM. This study offers novel perspectives on the role of anion framework modifications in modulating lithium sublattice for enhanced ion transport. These findings advance the development of high-performance SEs for next-generation all-solid-state batteries.

4. Experimental Section

Material Synthesis

LiBr (Sigma Aldrich) was dried at 200 °C under dynamic vacuum for 12 h and subsequently stored in an argon-filled glovebox. Anhydrous Li_2S and $AlBr_3$ (Alfa Aesar) were used without further purification and handled under an inert atmosphere. The precursors, in stoichiometric ratios, were manually ground with a mortar and pestle for 5 min inside an argon-filled glovebox. The resulting mixture was then transferred to a ZrO_2 jar containing two 10-mm balls as milling media. After vacuum sealing, mechanochemical processing was carried out using a SPEX 8000M MIXER/MILL (SPEX SamplePrep, USA) for 10 h. The ball-milled powder (≈130 mg) was then compacted into 8 mm diameter pellets under ≈400 MPa within an argon-filled Mbraun glovebox.

PXRD

The milled samples were placed in a zero-background sample holder and sealed with KAPTON film (DUPONT, USA) to prevent moisture exposure. PXRD analysis was performed using a RIGAKU Smartlab diffractometer in Bragg–Brentano geometry, operating at 45 kV and 40 mA with Cu-Kα radiation ($\lambda = 1.540562$ Å). Data was collected over a 2θ range of 10–80° with a step size of 0.03°.

Rietveld Refinement

Rietveld refinement of the laboratory PXRD data was carried out using GSAS-II software. Structural analysis of the PXRD data for $LiAlBr_4$ and $Li_{1.2}AlBr_{3.8}S_{0.2}$ confirmed a monoclinic phase within the $P2_1/a$ space group, consistent with $LiGaBr_4$ (ICSD – 61 337). Sulfur occupancy was evaluated across all chlorine sites, with results deemed reliable only when occupancy exceeded 1%. Lithium and aluminum site occupancies were examined by interchanging them at counter-cation positions to determine the most plausible structural arrangement. Atomic parameters for substituents (e.g., S, Br) were held fixed during refinement.

Computational Approach

Density functional theory (DFT) calculations and AIMD simulations were conducted using the Vienna Ab initio Simulation Package (VASP).[44] The projector-augmented wave (PAW) method[45] and Perdew–Burke–Ernzerhof generalized gradient approximation were applied for exchange–correlation interactions. The most recent PAW potential files in VASP were utilized.[46] Structural optimization of $Li_{1.2}AlBr_{3.8}S_{0.2}$ was performed using the Python Materials Genomics (Pymatgen) package.[47] A total of ten unique supercells were generated from a 2 × 2 × 1 supercell based on XRD data. Geometry optimizations were executed via DFT calculations. AIMD simulations were conducted within the canonical ensemble for 80 ps with a 2 fs time step, with the temperature ramped from 100 K to the target simulation value.

Solid-State NMR

Li and ^{7}Li NMR measurements were carried out on a Bruker Avance-III 500 spectrometer at Larmor frequencies of 73.6 MHz for ^{6}Li and 194.4 MHz for ^{7}Li. Magic-angle spinning (MAS) was set at 24 kHz. Single-pulse MAS NMR experiments were conducted using $\pi/2$ pulse lengths of 3.25 μs for ^{6}Li and 3.04 μs for ^{7}Li. Recycle delays were 500 s for ^{6}Li and 60 s for ^{7}Li in $Li_{1.2}AlBr_{3.8}S_{0.2}$, while $LiAlBr_4$ was analyzed with recycle delays of 500 s for ^{6}Li and 70 s for ^{7}Li. ^{7}Li NMR spectra were referenced to solid LiCl at -1.1 ppm. The inversion-recovery pulse sequence was utilized to determine the ^{7}Li T_1 relaxation times.

VT ^{7}Li T_1 relaxation NMR experiments were conducted on a Bruker Avance-I 300 MHz spectrometer using an inversion recovery pulse sequence ($\pi/2$ pulse $= 2.63$ μs) at a ^{7}Li Larmor frequency of 116.6 MHz. Samples were packed in a 4 mm ZrO_2 rotor under argon and spun at 10 kHz MAS.

EIS

The samples were pressed into 1.3-mm-thick, 8-mm-diameter pellets and sandwiched between 6-mm indium foil and stainless steel plungers as ion-blocking electrodes. Potentiostatic EIS measurements were performed using a Biologic SP-300 analyzer across 7 MHz to 1 Hz. Conductivities were derived from Nyquist plot fitting with an equivalent circuit. Temperature-dependent EIS was conducted from 0 °C to 60 °C in a cincinnati sub-zero (CSZ) chamber, with activation energies determined from the Arrhenius-type plots.

DC Polarization

The electronic conductivity was determined using the DC polarization technique.[48] Custom-designed split cells (8-mm diameter) were constructed with a polyether ether ketone (PEEK) insulating cylinder and stainless-steel plungers as current collectors. Indium foils (6-mm-diameter) served as ion-blocking electrodes.

Cyclic Voltammetry and Galvanostatic Cycling of ASSB Half-Cells

All-solid-state half-cells were fabricated using custom-built pressure cells with a 10-mm PEEK casing and stainless-steel plungers. For Cyclic voltammetry (CV) measurements, ≈100 mg of either $LiAlBr_4$ or $Li_{1.2}AlBr_{3.8}S_{0.2}$ was initially compressed at 300 MPa for 10 s to form a SE pellet. A composite mixture of the SE and carbon black (Super P) in a 3:1 ratio (≈10 mg total) was manually blended, uniformly layered on one side of the pellet, and pressed again at 300 MPa for 10 s. On the opposite side of the pellet, a 5/16-inch diameter (0.1 mm thick) indium foil (≈32 mg) was placed, followed by a ≈1 mg lithium foil (3/16-inch diameter), pressed to form a Li–In alloy counter electrode. The final cell architecture was Li–In|SE|3SE:C. Each cell was sealed using vacuum grease and subjected to electrochemical testing under an estimated stack pressure of ≈30 MPa at room temperature (22 °C). CV was performed from 0 to 5 V versus Li–In at a scan rate of 0.2 mV s^{-1}.

The composite cathode for galvanostatic cycling was prepared by drying TiS_2 (Sigma Aldrich, 99.9%) at 200 °C for 12 h, followed by ball milling at 300 rpm for 5 h to reduce particle size. The TiS_2 was then mixed with either $LiAlBr_4$ or $Li_{1.2}AlBr_{3.8}S_{0.2}$ in a 1:2 mass ratio and manually ground for 10 min. Li_6PS_5Cl, synthesized as per Patel et al.,[49] was pressed into pellets at 300 MPa for 10 s to serve as the SE separator. For assembly, 12 mg of the catholyte was uniformly applied to one side of the Li_6PS_5Cl pellet, achieving an areal capacity of ≈1.25 mAh cm^{-2}, and pressed again at 300 MPa. A Li–In alloy foil was attached to the opposite side to complete the Li-In|Li_6PS_5Cl|2SE:TiS_2 (SE: $LiAlBr_4$ or $Li_{1.2}AlBr_{3.8}S_{0.2}$) half-cell configuration. The cells were sealed with vacuum grease and cycled at 22 °C under ≈30 MPa stack pressure within a voltage range of 1–2.5 V versus Li–In. Rate capability tests were performed at 0.1C, 0.2C, 0.5C, 1C, and 2C (corresponding to 0.14, 0.28, 0.70, 1.40, and 2.80 mA cm^{-2}, respectively) for 5 cycles each, followed by long-term cycling at 0.2C for 75 cycles.

Acknowledgements

I.P.O. and T.P.P. contributed equally to this work. The authors acknowledge the support from the National Science Foundation under grant no. DMR-1847038. All solid-state NMR experiments were performed at the National High Magnetic Field Laboratory, which was supported by National Science Foundation Cooperative agreement nos. DMR-1644779 and DMR-2128556*.

Conflict of Interest

The authors declare no competing financial interest.

Data Availability Statement

The data that support the findings of this study are available from the corresponding author upon reasonable request.

Keywords: all-solid-state batteries · cycling stability · ionic conductivity · Li^{+} transport · migration energy barrier

[1] F. Jiang, Y.-F. Du, J.-X. Guo, N.-L. Shen, Z.-X. Chen, M. Geng, D. Ren, B.-Q. Li, X.-Q. Zhang, T. Wang, Y. Ma, Y. Zhong, J. He, Z. Zhu, F. Wang, J.-Q. Huang, X.-B. Cheng, Y. Wu, *Energy Environm. Sci.* **2025**, *18*, 4925.
[2] M. Lim, H. An, J. Seo, M. Lee, H. Lee, H. Kwon, H. T. Kim, D. Esken, R. Takata, H. A. Song, H. Lee, *Small* **2023**, *19*, e2302722.
[3] Y. E. Choi, K. H. Park, D. H. Kim, D. Y. Oh, H. R. Kwak, Y. G. Lee, Y. S. Jung, *ChemSusChem* **2017**, *10*, 2605.
[4] R. Guo, K. Zhang, W. Zhao, Z. Hu, S. Li, Y. Zhong, R. Yang, X. Wang, J. Wang, C. Wu, Y. Bai, *Energy Mater. Adv.* **2023**, *4*, 1.
[5] J. Chen, C. Hu, R. Liu, M. Hu, L. Li, Y. Zhang, X. Liu, L. Chen, *J. Phys. Chem. Lett.* **2025**, *16*, 731.
[6] Z.-X. Kong, Z. Xiong, J.-F. Wu, J. Jin, Y. Lin, Y. Li, J. Liu, *ACS Energy Lett.* **2024**, *10*, 287.
[7] N. L. Shen, F. Jiang, J. X. Guo, Y. F. Du, Z. Y. Qu, X. Shen, Y. Zhou, Z. Lyu, G. Xiao, X. B. Cheng, Y. Wu, *Adv. Funct. Mater.* **2025**, 2505437.
[8] W. Yu, N. Deng, Y. Feng, X. Feng, H. Xiang, L. Gao, B. Cheng, W. Kang, K. Zhang, *eScience* **2025**, *5*, 100278.
[9] S. Chen, D. Xie, G. Liu, J. P. Mwizerwa, Q. Zhang, Y. Zhao, X. Xu, X. Yao, *Energy Storage Mater.* **2018**, *14*, 58.
[10] Y.-T. Chen, M. A. T. Marple, D. H. S. Tan, S.-Y. Ham, B. Sayahpour, W.-K. Li, H. Yang, J. B. Lee, H. J. Hah, E. A. Wu, J.-M. Doux, J. Jang, P. Ridley, A. Cronk, G. Deysher, Z. Chen, Y. S. Meng, *J. Mater. Chem. A* **2022**, *10*, 7155.

[11] S. Cho, Y. Kim, Y. Song, J. Ryu, K. Choi, J. Yang, S. H. Lee, S. G. Im, S. Park, *Adv. Funct. Mater.* **2024**, *34*, 2314710.
[12] M. Gombotz, D. Rettenwander, H. M. R. Wilkening, *Front Chem* **2020**, *8*, 1.
[13] X. Feng, P.-H. Chien, S. Patel, J. Zheng, M. Immediato-Scuotto, Y. Xin, I. Hung, Z. Gan, Y.-Y. Hu, *Energy Storage Mater.* **2019**, *22*, 397.
[14] H. Li, Q. Lin, J. Wang, L. Hu, F. Chen, Z. Zhang, C. Ma, *Angew. Chem. Int. Ed. Engl.* **2024**, *63*, e202407892.
[15] K. Wang, Q. Ren, Z. Gu, C. Duan, J. Wang, F. Zhu, Y. Fu, J. Hao, J. Zhu, L. He, C. W. Wang, Y. Lu, J. Ma, C. Ma, *Nat. Commun.* **2021**, *12*, 1–11.
[16] V. Landgraf, M. Tu, W. Zhao, A. K. Lavrinenko, Z. Cheng, J. Canals, J. de Leeuw, S. Ganapathy, A. Vasileiadis, M. Wagemaker, T. Famprikis, *J. Am. Chem. Soc.* **2025**, *147*, 18840.
[17] F. N. Forrester, J. A. Quirk, T. Famprikis, J. A. Dawson, *Chem. Mater.* **2022**, *34*, 10561.
[18] Tufail, M. K.; Zhai, P.; Jia, M.; Zhao, N.; Guo, X., *Energy Mater. Adv.* **2023**, *4*, 1.
[19] W. Zhao, J. Yi, P. He, H. Zhou, *Electrochem. Energy Rev.* **2019**, *2*, 574–605.
[20] Y. Wang, W. D. Richards, S. P. Ong, L. J. Miara, J. C. Kim, Y. Mo, G. Ceder, *Nat. Mater.* **2015**, *14*, 1026.
[21] S. Sradhasagar, S. Pati, A. Roy, *J. Phys.Chem. C* **2024**, *128*, 15242.
[22] N. Flores-Gonzalez, N. Minafra, G. Dewald, H. Reardon, R. I. Smith, S. Adams, W. G. Zeier, D. H. Gregory, *ACS Mater. Lett.* **2021**, *3*, 652.
[23] T. P. Poudel, I. P. Oyekunle, M. J. Deck, Y. Chen, D. Hou, P. K. Ojha, B. Ogbolu, O. C. Huang, H. Xiong, Y. Y. Hu, *Chem. Sci.* **2025**, 2391.
[24] R. Miyazaki, M. Nakayama, T. Hihara, *J. Solid State Electrochem.* **2024**, *29*, 585.
[25] T. Song, Y. Lin, D. Wang, Q. Chen, C. Ling, S. Shi, *Adv. Energy Mater.* **2024**, *14*, 2302440.
[26] Y. Chen, P. Wang, E. Truong, B. Ogbolu, Y. Jin, I. Oyekunle, H. Liu, M. M. Islam, T. Poudel, C. Huang, I. Hung, Z. Gan, Y. Y. Hu, *Angew. Chem. Int. Ed. Engl.* **2024**, *63*, e202408574.
[27] S. V. Patel, E. Truong, H. Liu, Y. Jin, B. L. Chen, Y. Wang, L. Miara, R. Kim, Y.-Y. Hu, *Energy Storage Mater.* **2022**, *51*, 88.
[28] B. B. Duff, S. J. Elliott, J. Gamon, L. M. Daniels, M. J. Rosseinsky, F. Blanc, *Chem. Mater.* **2023**, *35*, 27.
[29] P. Wang, S. Patel, H. Liu, P. H. Chien, X. Feng, L. Gao, B. Chen, J. Liu, Y. Y. Hu, *Adv. Funct. Mater.* **2023**, *33*, 2307954.
[30] N. Bloembergen, E. M. Purcell, R. V. Pound, *Phys. Review* **1948**, *73*, 679.
[31] I. P. Oyekunle, E. Truong, T. P. Poudel, Y. Chen, Y. Jin, I. A. Ojelade, M. J. Deck, B. Ogbolu, M. M. Islam, P. K. Ojha, J. S. R. Vellore Winfred, D. Hou, H. Xiong, C. Huang, Y. Y. Hu, *Chem. Sci.* **2025**, *16*, 10372.
[32] E. Truong, S. V. Patel, H. Liu, Y. Chen, V. Lacivita, C. Zhang, I. P. Oyekunle, I. Ojelade, Y. Jin, B. T. Jones, L. J. Miara, V. P. Dravid, H. Gao, R. Kim, Y. Wang, Y.-Y. Hu, *Sci. Adv.* **2025**, *11*, eadt7795.
[33] P. Wang, H. Liu, S. Patel, J. E. Roberts, Y. Chen, B. Ogbolu, B. E. Francisco, Y. Y. Hu, *Adv. Energy Mater.* **2024**, *14*, 2401549.
[34] P.-H. Chien, K. J. Griffith, H. Liu, Z. Gan, Y.-Y. Hu, *Annu. Rev. Mater. Res.* **2020**, *50*, 493.
[35] T. P. Poudel, E. Truong, I. P. Oyekunle, M. J. Deck, B. Ogbolu, Y. Chen, P. K. Ojha, T. N. D. D. Gamaralalage, S. V. Patel, Y. Jin, D. Hou, C. Huang, T. Li, Y. Liu, H. Xiong, Y.-Y. Hu, *ACS Energy Lett.* **2024**, *10*, 40.
[36] T. P. Poudel, M. J. Deck, P. Wang, Y. Y. Hu, *Adv. Funct. Mater.* **2023**, *34*, 2309656.
[37] R. Schlem, A. Banik, M. Eckardt, M. Zobel, W. G. Zeier, *ACS Appl. Energy Mater.* **2020**, *3*, 10164.
[38] R. Schlem, A. Banik, S. Ohno, E. Suard, W. G. Zeier, *Chem. Mater.* **2021**, *33*, 327.
[39] W. D. Richards, L. J. Miara, Y. Wang, J. C. Kim, G. Ceder, *Chem. Mater.* **2015**, *28*, 266.
[40] S. H. Akella, M. Bagavathi, D. Rosy Sharon, C. Ozgur, M. Noked, *J. Mater. Chem. A* **2023**, *11*, 20480.
[41] X. Li, Y. Wang, J. Lu, P. Li, Z. Huang, G. Liang, H. He, C. Zhi, *Science Adv.* **2024**, *10*, eadl0587.
[42] M. J. Deck, P. H. Chien, T. P. Poudel, Y. Jin, H. Liu, Y. Y. Hu, *Adv. Energy Mater.* **2023**, *14*, 2302785.
[43] B. O. Ogbolu, T. P. Poudel, T. Dikella, E. Truong, Y. Chen, D. Hou, T. Li, Y. Liu, E. Gabriel, H. Xiong, C. Huang, Y. Y. Hu, *Adv Sci Weinh* **2024**, e2409668.
[44] G. Kresse, J. Furthmuller, *Phys. Rev. B* **1996**, *54*.
[45] P. E. Blochl, *Phys. Rev. B Condens. Matter.* **1994**, *50*, 17953.
[46] J. P. Perdew, K. Burke, M. Ernzerhof, *Phys. Rev. Lett.* **1996**, *77*, 3865.
[47] S. P. Ong, W. D. Richards, A. Jain, G. Hautier, M. Kocher, S. Cholia, D. Gunter, V. L. Chevrier, K. A. Persson, G. Ceder, *Comput. Mater. Sci.* **2013**, *68*, 314.
[48] S. Ohno, C. Rosenbach, G. F. Dewald, J. Janek, W. G. Zeier, *Adv. Funct. Mater.* **2021**, *31*, 2010620.
[49] S. V. Patel, S. Banerjee, H. Liu, P. Wang, P.-H. Chien, X. Feng, J. Liu, S. P. Ong, Y.-Y. Hu, *Chem. Mater.* **2021**, *33*, 1435.

Manuscript received: June 7, 2025
Revised manuscript received: July 21, 2025
Version of record online: August 9, 2025